

Supplementary Information

For

***In-situ* synthesis of silicon flake/nitrogen-doped graphene-  
like carbon composite from organoclay for high-  
performance lithium-ion battery anode**

Qingze Chen<sup>a, b</sup>, Runliang Zhu<sup>a\*</sup>, Qiuzhi He<sup>a, b</sup>, Shaohong Liu<sup>c</sup>, Dingcai Wu<sup>c\*</sup>,

Haoyang Fu<sup>a, b</sup>, Jing Du<sup>a, b</sup>, Jianxi Zhu<sup>a</sup>, Hongping He<sup>a, b</sup>

<sup>a</sup> CAS Key Laboratory of Mineralogy and Metallogeny, Guangdong Provincial Key Laboratory of Mineral Physics and Materials, Guangzhou Institute of Geochemistry, Chinese Academy of Sciences, Guangzhou 510640, China

<sup>b</sup> University of Chinese Academy of Sciences, Beijing 100049, China

<sup>c</sup> Materials Science Institute, PCFM Lab and GDHPRC Lab, School of Chemistry, Sun Yat-sen University, Guangzhou, P. R. China

\* Corresponding author

Prof. Runliang Zhu, E-mail: zhurl@gig.ac.cn

Prof. Dingcai Wu, E-mail: wudc@mail.sysu.edu.cn

## Experimental Details

### Materials

The raw montmorillonite (Mt) with a purity > 95% was obtained from Inner Mongolia, China. Its cation-exchange capacity (CEC) measured by the adsorption of  $[\text{Co}(\text{NH}_3)_6]^{3+}$  was 110.5 mmol/100 g.<sup>1</sup> The chemical composition was listed as follows: SiO<sub>2</sub> 58.16%, Al<sub>2</sub>O<sub>3</sub> 16.95%, Fe<sub>2</sub>O<sub>3</sub> 5.26%, MgO 3.57%, CaO 2.29%, Na<sub>2</sub>O 0.19%, K<sub>2</sub>O 0.15%, MnO 0.03%, TiO<sub>2</sub> 0.2%, P<sub>2</sub>O<sub>5</sub> 0.08%, and the ignition loss 13.12%. Anhydrous aluminum chloride (AlCl<sub>3</sub>) and aluminum powder (Al) were of analytical grade and purchased from Shanghai Aladdin Chemical Reagent Co., Ltd. The cationic dye, crystal violet (CV), was of analytical grade and supplied by Shanghai Chemical Reagent Factory, China. Hydrochloric acid (HCl, 37 wt.%) and hydrofluoric acid (HF, 40 wt.%) were obtained from Guangzhou Chemical Reagent Factory, China.

### Materials synthesis

The synthesis of montmorillonite/carbon composite (Mt/C): 10 g of Mt was added into a 1000 mL of CV solution with a concentration of 1 g/L. The suspension was vigorously agitated for 6 h at room temperature, and then centrifuged at 4000 rpm to separate the products. The CV was almost adsorbed completely on Mt, which was verified by the very low concentration of CV in the supernatant detected *via* a ultraviolet-visible spectrophotometer. This above adsorption amount of crystal violet on Mt, equivalent to 0.22 CEC of Mt, was selected in order to control the C content in the resulting Si product. The sediment was collected and dried at 60°C overnight (made as Mt/CV). Subsequently, Mt/CV was pyrolyzed at 700°C for 3 h under a N<sub>2</sub>

flow in a tube furnace. The resulting products (Mt/C) was collected for the following experiment.

The synthesis of silicon flake/nitrogen-doped graphene-like carbon composite (Si/NG): Typically, 1 g of Mt/C, 0.6 g of Al, and 10 g AlCl<sub>3</sub> were uniformly mixed and sealed into a stainless steel reactor in an argon-filled glovebox. Then, this reactor was placed in the middle of the oven (Memert, Germany) and heated to 270°C at a slow rate (~2°/min) and held for 10 h. After cooling down naturally, the obtained mixtures were rinsed with 1 mol/L HCl for 3 h to eliminate the byproducts (e.g., AlOCl) and residual reagents, and then leached with 1% HF. After washing thoroughly with ethylalcohol and distilled water, the resulting Si/NG was vacuum-dried at 60°C overnight. As a control experiment, bare Si was prepared using the raw Mt as precursor under the same experimental conditions.

### **Characterization**

XRD patterns of the samples were measured using a Bruker D8 ADVANCE X-ray diffractometer (Bruker AXS, Germany) with a Ni filter and CuK $\alpha$  radiation ( $\lambda = 0.154$  nm) at 40 kV and 40 mA. SEM images and EDS data of the resulting products were determined on an SU-8010 cold field emission scanning electron microscope (Hitachi, Japan). TEM images and HRTEM images were obtained on an FEI Talos F200S field-emission transmission electron microscope (FEI Co., USA) at an acceleration voltage of 200 kV. Raman spectra were performed on a Renishaw 2000 confocal micro-Raman Spectrometer (Renishaw, UK) with an Ar-ion laser ( $\lambda = 514.5$  nm). TG analysis was carried out on a STA 409PC synchronization thermal analyzer (NETZSCH, Germany). The samples loaded in a corundum crucible were heated from 30 to 1000°C at a rate of 10°C min<sup>-1</sup> under a constant flow of dry air. XPS spectra were recorded on a Thermo K-Alpha XPS instrument (Thermo Fisher Scientific, UK)

equipped with a monochromatic Al-K $\alpha$  X-ray source (1468.6 eV). N<sub>2</sub> adsorption-desorption isotherms were collected on an ASAP 2020 system (Micromeritics Inc., USA) at liquid nitrogen temperature (77K). The specific surface area and pore size distribution of the sample were calculated using the multi-point Brunauer–Emmett–Teller (BET) equation and the Barrett-Joyner-Halenda (BJH) method, respectively. The corresponding total pore volume was achieved based on N<sub>2</sub> adsorption capacity at a relative pressure  $\sim$ 0.97.

### **Electrochemical measurements.**

The working electrode was prepared as follows: first, the as-prepared products, sodium alginate (SA, analytical grade) binder, and conductive agent (Super P) were fine mixed at a mass ratio of 8: 1: 1 in distilled water; thereafter, the resulting slurry was carefully blade-coated on a current collector (copper foil) and vacuum-dried at 60°C overnight to remove moisture. The mass loading density of active material was 0.8~1.0 mg cm<sup>-2</sup>. The electrochemical properties of the samples (Si/NG and bare Si) were evaluated in CR2032 coin half cells assembled in an argon-filled glovebox (less than 0.1 ppm of both water and oxygen) with lithium foils as the reference and counter electrodes. For coin-type cell fabrication, the cast electrodes were cut into disks as working electrodes, and the Celgard 2400 polyethylene porous membranes as separators. 1 M LiPF<sub>6</sub> in 1:1 (by volumetric ratio) ethylene carbonate/dimethyl carbonate (EC/DMC) with 10 wt.% fluorinated ethylene carbonate (FEC) was employed as electrolyte. The rate capability and cycling stability of the electrodes were performed on a LAND-CT2001A multichannel battery-testing instrument at various current densities within a voltage range from 0.001 to 1.5 V. Cyclic voltammetry were carried out on a CHI660D electrochemical workstation (Chenhua Instrument Co., Ltd., China) in the voltage range of 0.001–1.5 V at a scan rate of 0.1

mV s<sup>-1</sup>. The electrochemical impedance spectroscopy (EIS) was also obtained in the same apparatus in the frequency range of 0.01-100 kHz with an alternating current perturbation of 5 mV. The gravimetric capacity was calculated on the basis of active materials only. After electrochemical measurements, we disassembled the cells in an argon-filled glovebox, and completely rinsed the working electrodes with dimethyl carbonate for further characterization.

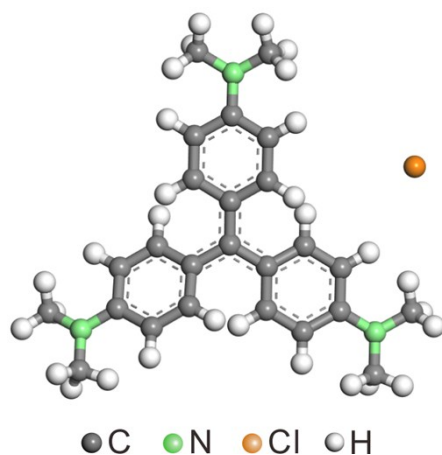


**Fig. S1** The structure of Crystal violet (CV). CV is a typical cationic dye with the chemical formula of  $C_{24}H_{28}N_3Cl$ .

Crystal violet (known as methyl violet 10B) was selected in our study for the following reasons: 1) it had a good cationic exchange ability, allowing it to intercalate into the interlayer space of Mt; 2) it can be used as both C and N sources; 3) the benzene ring in crystal violet could be easily transformed to graphene-like carbon within the interlayer space. Based on the above considerations, other types of methyl violet (i.e., methyl violet 2B, methyl violet 6B) can be theoretically used as precursors like crystal violet.

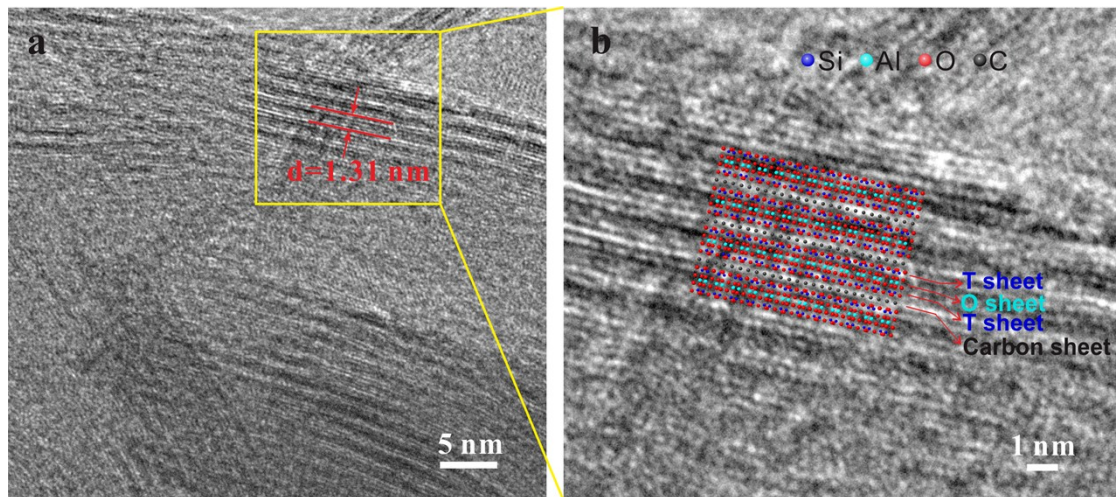


**Fig. S2** High-resolution TEM image (a) and an enlarged view along with a structural model (b) of Mt/C.

The high-resolution TEM image of Mt/C clearly showing the alternating structures composed of Mt layer and carbon layer.

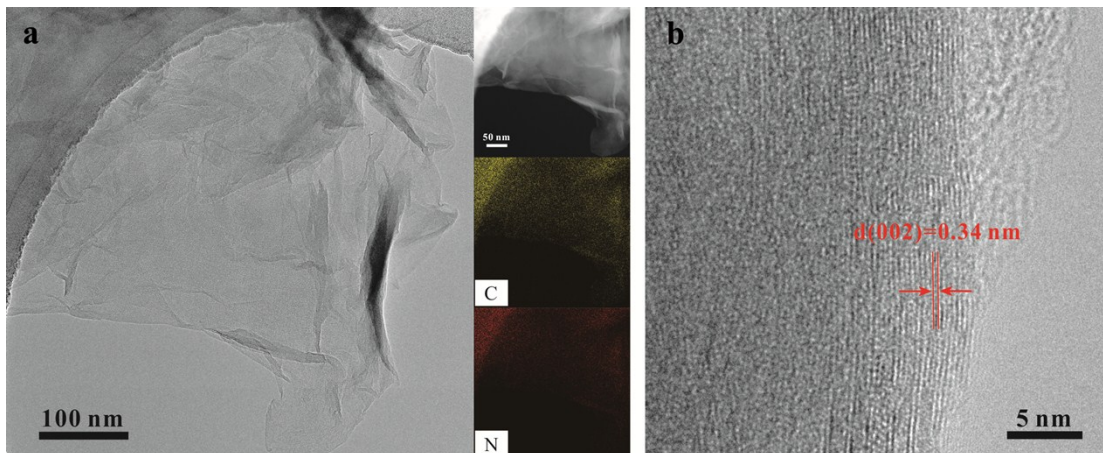


**Fig. S3** Characterization of the resulting carbon materials after the removal of the Mt layers from Mt/C (by washing with HCl and HF). (a) TEM image and EDS mapping, (b) high-resolution TEM image showing typical (002) spacing.

The TEM image of the carbon material after the removal of Mt layers (Fig. S3, ESI†) further confirmed the formation of a graphene-like carbon sheet within the confined interlayer space of Mt. According the corresponding energy dispersive X-ray spectroscopy (EDS), the content of N atoms in NG was about 5.5 at.%.

It is believed that N-doping into the carbon materials (e.g., graphene) can modify the structure of neighbor C atoms and provide a large number of surface defects and active sites, enhancing the reaction kinetics of carbon electrodes.<sup>2, 3</sup> Besides, the incorporation of N atoms into carbon can also improve electrical conductivity and interfacial stability due to remarkable electron transfer from the electroactive materials to carbon.<sup>2, 3</sup> As such, N-doped graphene-like material in our work as a promising coating agent for Si can increase electronic conductivity and active sites toward lithium, thus realizing an excellent electrochemical properties.

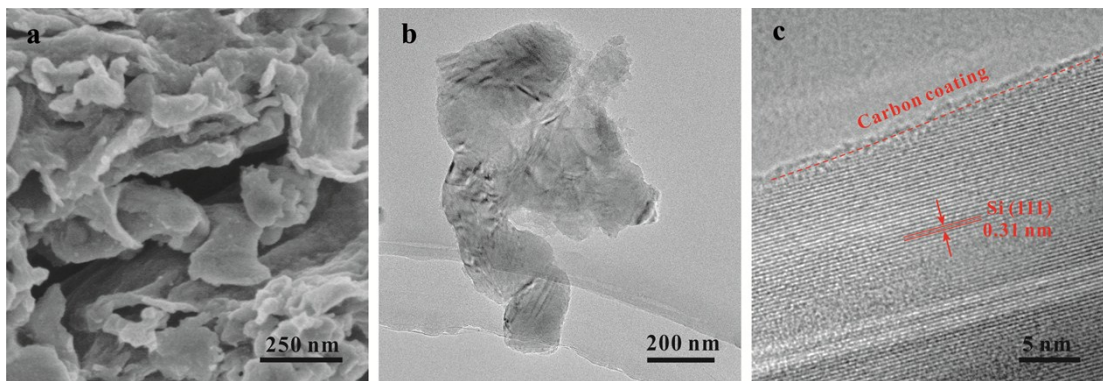


**Fig. S4** High-magnification SEM image (a), low-magnification TEM image (b) and HRTEM image showing the crystalline silicon coated with less than 1-nm-thick carbon layers (c) of Si/NG.

Both SEM and TEM images clearly indicated the lamellar morphology of Si/NG (Fig. S4a and b, ESI†). The HRTEM images showing the crystalline Si coated with 4-nm-thick (Fig. 3) and less than 1-nm-thick carbon layers (Fig. S4c, ESI†), while a 0.35-nm-thick graphene-like carbon layer was observed inside the alternating structure of Mt/C (Fig. S2, ESI†). These results suggested that carbon monolayers experienced a reassembly process during the thermal reduction reaction (to lower the surface energy).

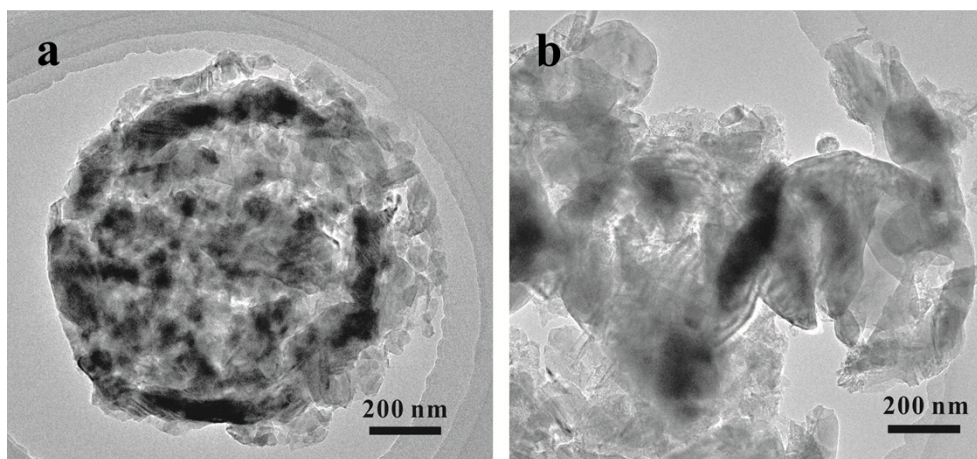


**Fig. S5** TEM image of Si product synthesized from the initial mixture of 1 g of Mt, 1.2 g of Al, and 20 g  $\text{AlCl}_3$  (a) and from the initial mixture of 1 g of Mt, 0.6 g of Al, and 10 g  $\text{AlCl}_3$  (b).

According to the previous works,<sup>4, 5</sup> the formation of hollow Si nanostructure was greatly influenced by the experimental parameters and preparation conditions, such as the reaction temperature, the amount of reagents, and the size of Al powder. Moreover, the introduction of the carbon coating could contribute to the preservation of original morphology during the reduction reaction (e.g., the spherical shape<sup>6</sup> or spherical shell<sup>7</sup>). The use of binary or eutectic salts in these works also helped stabilize the reaction medium (e.g., to lower the pressure of  $\text{AlCl}_3$  for easy handling, or to decrease the melting point of the mixture). These wonderful studies were helpful for us to understand the controlled synthesis of hollow Si nanostructure by the low-temperature aluminothermic reduction.

In our work, the fragments for hollow and porous microsphere were observed in the TEM image of bare Si (Fig. S5b, ESI<sup>†</sup>), consistent with the SEM image (Fig. 2e). Furthermore, we synthesized a new bare Si by increasing the amount of reductant (i.e., using the initial mixture of 1 g of Mt, 1.2 g of Al, and 20 g  $\text{AlCl}_3$ ), according to a high amount of reductant used in previous studies.<sup>4</sup> The resulting Si product exhibited a morphology of intact hollow Si sphere, as shown by the TEM image (Fig. S5a, ESI<sup>†</sup>).

This phenomenon was also in well agreement with the previous reports.<sup>4, 5</sup> By contrast, Si/NG showed a lamellar morphology (i.e., nanoflake), totally different from bare Si, which indicated the role of carbon layers as isolation barriers.

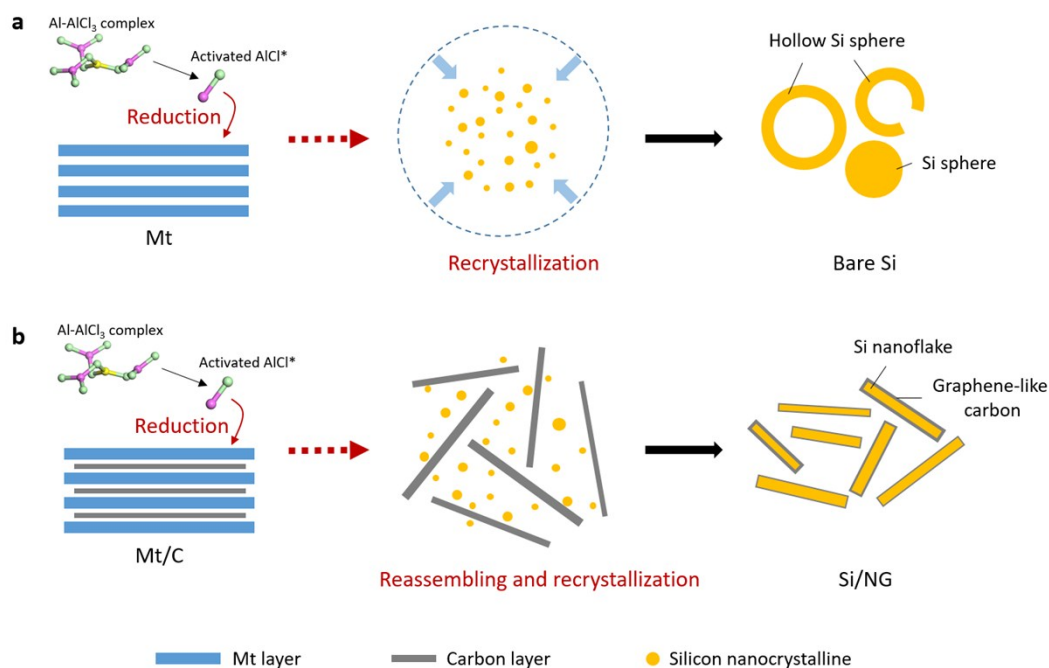


**Fig. S6** Schematic illustration of the formation processes of bare Si (a) and Si/NG (b).

Based on the results in our work and previous studies<sup>4-7</sup>, we have provided a probable reaction mechanism from Mt/C to Si/NG as follows:

First, activated AlCl\* was generated from the ligand of the Al–AlCl<sub>3</sub> complex (Fig. S6, ESI†),<sup>5</sup> and then attacked the strong Si–O bond on the surface and end face of Mt. Meanwhile, Mt and Mt/C were exfoliated and dispersed in the molten salt systems,<sup>8,9</sup> leading to more sufficient contact with AlCl\*. The Si–O tetrahedra of Mt were reduced by activated AlCl\* to Si seeds, while the carbon layers reassembled in the molten salt medium to decrease the surface energy. In the absence of carbon layers, the Si seeds became recrystallized into spherical shells or spherical particles *via* localized Ostwald ripening process as the reaction progressed (Fig. S6a, ESI†).<sup>4,5</sup> By contrast, the *in-situ* introduction of carbon layers made a kind of barrier to excessive clustering of Si nanocrystals. More importantly, the carbon layers could act as nanotemplates to induce the newly formed Si nanocrystals to grow into Si flakes, resulting in the formation of Si/NG (Fig. S6b, ESI†).

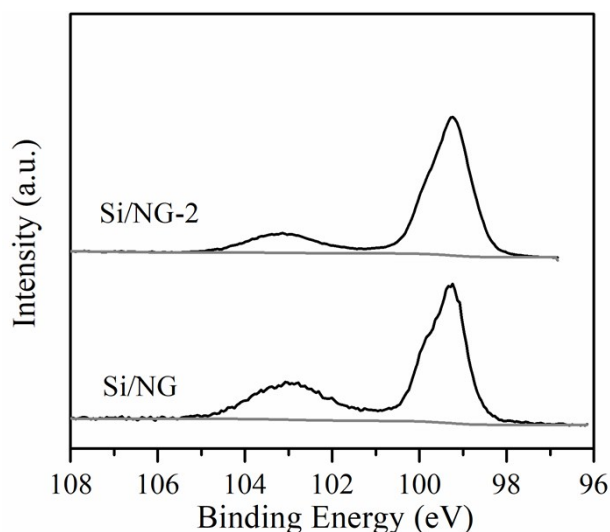


**Fig. S7** High resolution Si2p XPS spectra of Si products (marked as Si/NG-2) synthesized using an enhanced amount of reductant (i.e., the initial mixture of 1 g of Mt/C or Mt, 1.2 g of Al, and 20 g AlCl<sub>3</sub>). For comparison, the high resolution Si2p XPS spectra of Si/NG was adopted from Fig. 4c.

The high resolution Si2p XPS spectrum showed the content of SiO<sub>x</sub> derivatives in Si/NG-2 was less than that of Si/NG (Fig. S7, ESI†), which suggested the more complete reduction reaction with increasing the amount of reductant. These results indicated that the SiO<sub>x</sub> derivatives could be derived from the incomplete reduction of Si-O tetrahedra besides from the post-oxidation of the obtained Si products. The similar phenomena were also reported in previous studies on the synthesis of Si nanostructures.<sup>6, 10</sup>

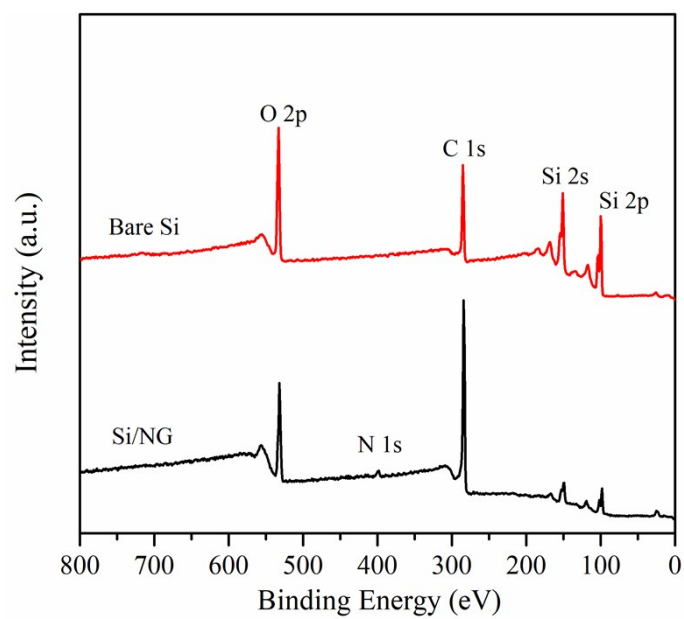


**Fig. S8** XPS survey spectra of Si/NG and bare Si.

XPS survey spectra of Si/NG showed the absence of other metal elements, which manifested a high-purity of Si/NG.

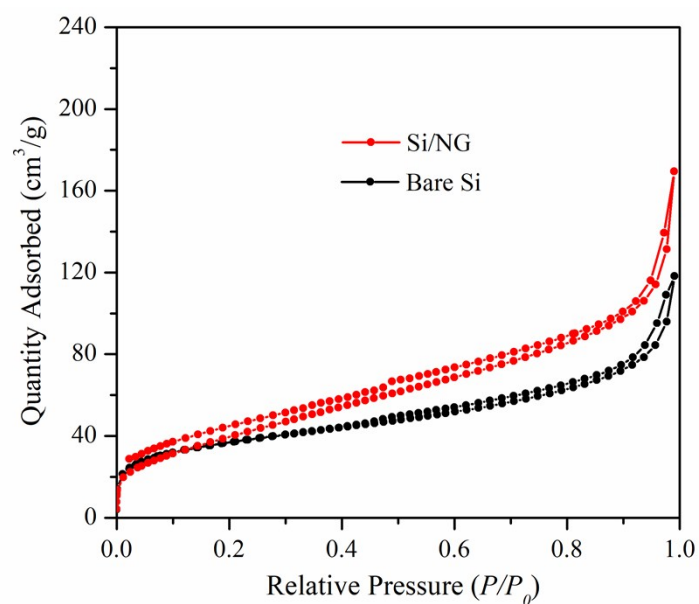


**Fig. S9** N<sub>2</sub> adsorption-desorption isotherms of Si/NG and bare Si.

The N<sub>2</sub> adsorption/desorption isotherms showed that both Si/NG and bare Si possessed II-type isotherms according to the IUPAC classification, indicative of macroporous characteristics.<sup>11</sup> The very little adsorption capacity of N<sub>2</sub> in low relative pressure range and the inconspicuous hysteresis loops in middle relative pressure range implied a small number of micropores and mesopores; while the sharp increase of isotherms in the high relative pressure range further confirmed a number of macropores. In addition, Si/NG had better N<sub>2</sub> adsorption capacity in the middle and high relative pressure ranges, indicating a better developed pore system.

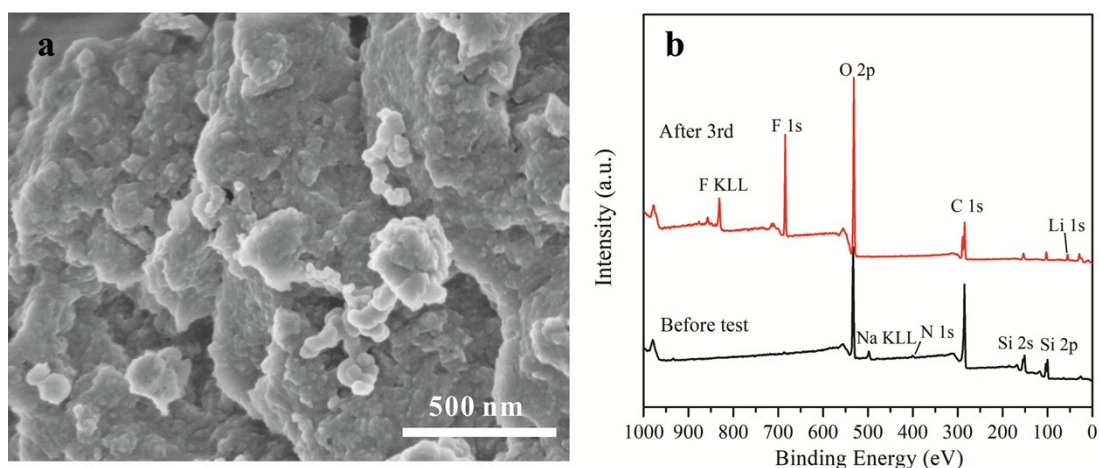


**Fig. S10** (a) SEM image of Si/NG after 3 cycles, (b) XPS survey spectra of the Si/NG electrodes before electrochemical test and after 3 cycles.

The SEM image indicated that Si/NG after 3 cycles was covered by an organic polymeric/gel-like layer (Fig. S10a), totally different from the fresh surface of Si/NG, which directly verified the formation of SEI films. Moreover, the XPS survey spectrum of Si/NG after 3 cycles showed the presence of F and Li (besides Si and C) and the significant increase in the O2p intensity compared to that of Si/NG before test (Fig. S10b), which were attributed to the SEI films composed of LiF,  $\text{Li}_x\text{SiO}_y$ , and a polymeric species (containing C–O and O–(C=O)–O bonds).<sup>12, 13</sup>

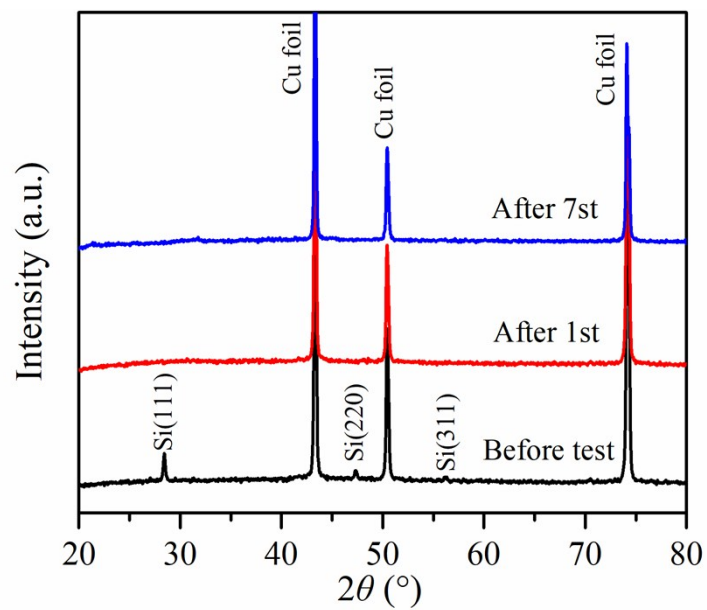


**Fig. S11** *Ex situ* XRD patterns of the Si/NG electrodes before electrochemical test and after different cycles at a scan rate of  $0.1 \text{ mV s}^{-1}$ .

The XRD patterns showed that the characteristic reflections of crystalline Si were visible before electrochemical test but disappeared after cycling, clearly revealing the transformation of crystalline Si to an amorphous phase during the first cycle.

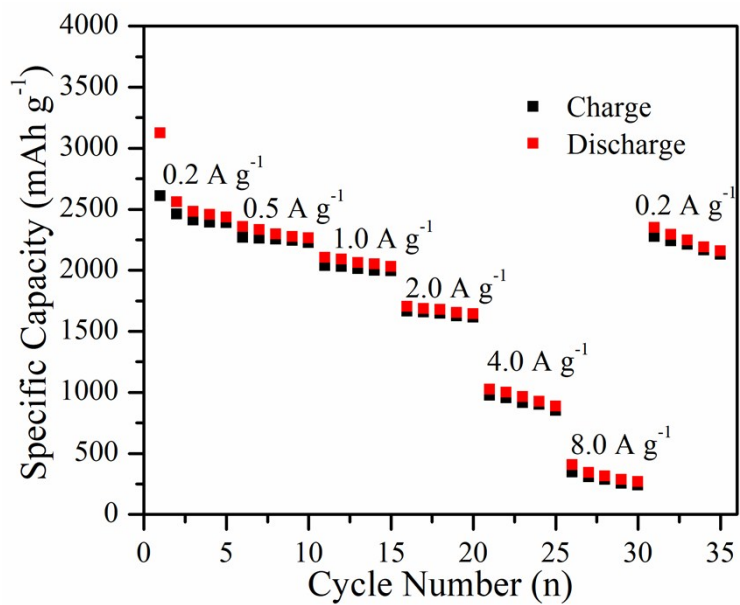


**Fig. S12** Rate capability of the bare Si electrode at various current densities from 0.2 to 8.0 A g<sup>-1</sup>.

Compared to Si/NG electrode, the bare Si electrode exhibited inferior rate performance, especially at large current densities.

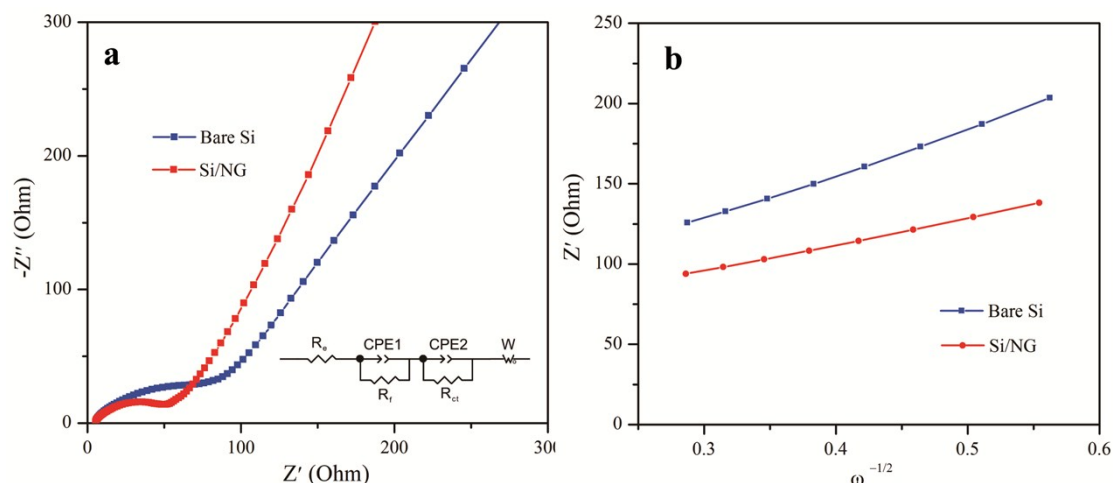


**Fig. S13** (a) Nyquist plots of the Si/NG and bare Si electrodes after 3 cycles (insert: the corresponding equivalent circuit;  $R_e$  represents the electrolyte resistance;  $R_f$  represents the resistance in the interface of the SEI film;  $R_{ct}$  represents the charge transfer resistance on electrode/electrolyte interface;  $W$  represents the Warburg impedance for the solid state diffusion of lithium ions; CPE1 and CPE2 represent the two resistors with constant phase elements)<sup>14</sup>. (b) The relationship between  $Z'$  and  $\omega^{-1/2}$  in the low frequency region.

The fitted data based on the equivalent circuit exhibited that the Si/NG and bare Si electrodes after 3 cycles possessed the  $R_{ct}$  values of 29 and 78  $\Omega$  (Fig. S13a, ESI<sup>†</sup>), respectively, which indicated the faster charge transfer kinetics for the Si/NG electrode. Furthermore, the relationship between  $Z'$  and  $\omega^{-1/2}$  in the low frequency region were plotted (Fig. S13b, ESI<sup>†</sup>). The slope of the curve represented the Warburg coefficient ( $\sigma_w$ ), proportional inversely to the diffusivity of lithium ions.<sup>15</sup> The calculated  $\sigma_w$  values for the Si/NG and bare Si electrodes after 3 cycles were 168 and 283  $\Omega \text{ s}^{-1/2}$ , respectively. The smaller  $\sigma_w$  of the Si/NG electrode suggested the better diffusion of lithium ions than bare Si electrode.

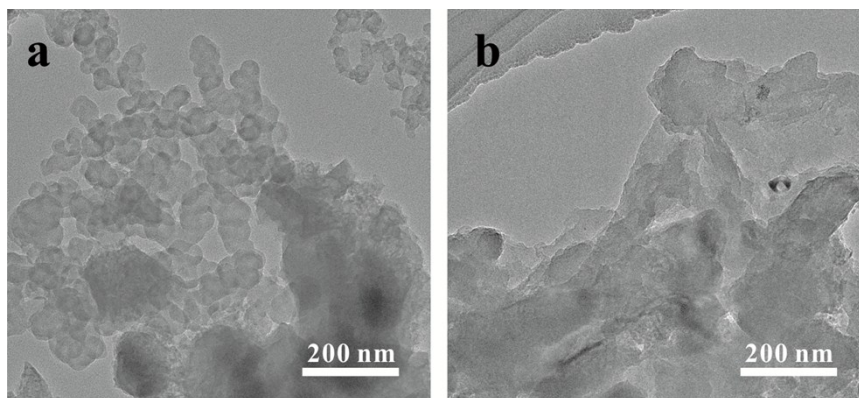


**Fig. S14** TEM images of bare Si (a) and Si/NG (b) after cycling 100 times.

TEM images of electrodes after cycling showed that both bare Si and Si/NG exhibited the large volume change and became amorphous. However, compared with bare Si, Si/NG did not break into smaller particles and kept the original morphology after cycling, suggesting the better structural/interfacial stability of Si/NG during cycling.

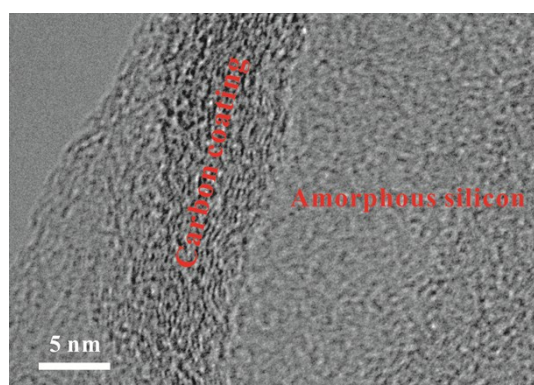


**Fig. S15** High-magnification TEM image of Si/NG after cycling 100 times.

No obvious separation in the interface between silicon and carbon was visible in the TEM image, suggesting a good interfacial stability of Si/NG during cycling.

**Table S1** Summary for electrochemical performances of nanostructured Si/C composite anodes synthesized by various methods in this work and in previous studies.

Si-based anodes	Rate performance	Cycle performance	Loading mass (mg/cm <sup>2</sup> )	ICE <sup>a</sup>	Methods	precursors	Ref.
Si/NG	434 mAh g <sup>-1</sup> at 8.0 A g <sup>-1</sup>	~1138 mAh g <sup>-1</sup> at 1.0 A g <sup>-1</sup> after 240 cycles	0.8~1.0	80%	Carbonization followed by low-temperature aluminothermic reduction	Organoclay	This work
Si@N-doped graphene cage	890 mAh g <sup>-1</sup> at 5.0 A g <sup>-1</sup>	~900 mAh g <sup>-1</sup> at 1.0 A g <sup>-1</sup> after 200 cycles	-	55%	Magnesiothermic reduction followed by chemical vapor deposition	Commercially available colloidal silica and acetonitrile	16
3D porous Si/N-doped carbon composite	360 mAh g <sup>-1</sup> at 1.6 A g <sup>-1</sup>	603 mAh g <sup>-1</sup> at 0.2 A g <sup>-1</sup> after 120 cycles	~1.5	68%	Calcination and magnesiothermic reduction followed by carbonization	Bamboo Charcoal and polyacrylonitrile	17
N-doped graphene enwrapped Si@N-doped carbon	975 mAh g <sup>-1</sup> at 2.0 A g <sup>-1</sup>	938mAh g <sup>-1</sup> at 0.5 A g <sup>-1</sup> after 100 cycles	-	76%	Solution-mixing and carbonization	Commercial Si nanoparticles, glucosamine hydrochloride and graphene oxide	18
N-rich carbon/Si composite	572 mAh g <sup>-1</sup> at 5.0 A g <sup>-1</sup>	1000 mAh g <sup>-1</sup> at 2.0 A g <sup>-1</sup> after 300 cycles	~1.0	75%	Solution-mixing and carbonization	Nano-sized Si powder and melamine	19
Si@amorphous carbon@N-doped graphene	948 mAh g <sup>-1</sup> at 3.0 A g <sup>-1</sup>	~1200 mAh g <sup>-1</sup> at 2.0 A g <sup>-1</sup> after 110 cycles	~1.2	75%	Freeze-drying and carbonization	Si nanoparticles, dopamine hydrochloride, and graphene oxide	20
Carbon coated Si nanosheet	670 mAh g <sup>-1</sup> at 2.0 A g <sup>-1</sup>	865 mAh g <sup>-1</sup> at 1.0 A g <sup>-1</sup> after 200 cycles	~1.5	79%	Molten salt-assisted magnesiothermic reduction followed by chemical vapor deposition	Montmorillonite and acetylene	8
Si@C@void@C	1009 mAh g <sup>-1</sup> at 4.0 A g <sup>-1</sup>	1366 mAh g <sup>-1</sup> at 0.5 A g <sup>-1</sup> after 50 cycles	~0.8	64%	Solution-mixing and carbonization twice	Si nanoparticles, dopamine hydrochloride, and tetraethoxysilane	21
Carbon coated Si nanotubes	1900 mAh g <sup>-1</sup> at 0.4 A g <sup>-1</sup>	~900 mAh g <sup>-1</sup> at 0.4 A g <sup>-1</sup> after 90 cycles	-	-	Electrospinning and magnesiothermic reduction followed by diazotization and carbonization	Tetraethoxysilane and p-phenylenediamine	22
Si/N-doped carbon/carbon nanotube spheres	978 mAh g <sup>-1</sup> at 1.0 A g <sup>-1</sup>	1380 mAh g <sup>-1</sup> at 0.5 A g <sup>-1</sup> after 100 cycles	0.8~1.0	72%	A polyacrylonitrile assisted electrospray method followed by carbonization	Rice husk, carbon nanotube, and polyacrylonitrile	23
Carbon coated porous Si	460 mAh g <sup>-1</sup> at 3.2 A g <sup>-1</sup>	~1124 mAh g <sup>-1</sup> at 0.4 A g <sup>-1</sup> after 100 cycles	0.8~1.2	-	Mechanical milling followed by thermal treatment under an Ar/CO <sub>2</sub> flow	Mg <sub>2</sub> Si and CO <sub>2</sub>	24

<sup>a</sup> Initial Coulombic efficiency

## References

1. L. Zhu, R. Zhu, L. Xu and X. Ruan, *Colloids Surf., A*, 2007, **304**, 41-48.
2. K. N. Wood, R. O'Hayre and S. Pylypenko, *Energy Environ. Sci.*, 2014, **7**, 1212-1249.
3. A. L. M. Reddy, A. Srivastava, S. R. Gowda, H. Gullapalli, M. Dubey and P. M. Ajayan, *ACS Nano*, 2010, **4**, 6337-6342.
4. Z.-W. Zhou, Y.-T. Liu, X.-M. Xie and X.-Y. Ye, *Chem. Commun.*, 2016, **52**, 8401-8404.
5. G. Song, J. Ryu, J. C. Kim, J. H. Lee, S. Kim, C. Wang, S. K. Kwak and S. Park, *Commun. Chem.*, 2018, **1**, 42.
6. K. Mishra, J. Zheng, R. Patel, L. Estevez, H. Jia, L. Luo, P. Z. El-Khoury, X. Li, X.-D. Zhou and J.-G. Zhang, *Electrochim. Acta*, 2018, **269**, 509-516.
7. P. Gao, X. Huang, Y. Zhao, X. Hu, D. Cen, G. Gao, Z. Bao, Y. Mei, Z. Di and G. Wu, *ACS Nano*, 2018, **12**, 11481-11490.
8. J. Ryu, D. Hong, S. Choi and S. Park, *ACS Nano*, 2016, **10**, 2843-2851.
9. Q.Z. Chen, R.L. Zhu, H.Y. Fu, L.Y. Ma, J.X. Zhu, H.P. He and Y.J. Deng, *Microporous Mesoporous Mater.*, 2018, **260**, 76-83.
10. K. Adpakpang, S. B. Patil, S. M. Oh, J.-H. Kang, M. Lacroix and S.-J. Hwang, *Electrochim. Acta*, 2016, **204**, 60-68.
11. M. Thommes, K. Kaneko, A. V. Neimark, J. P. Olivier, F. Rodriguez-Reinoso, J. Rouquerol and K. S. W. Sing, *Pure Appl. Chem.*, 2015, **87**, 1051-1069.
12. M. Nie, D. P. Abraham, Y. Chen, A. Bose and B. L. Lucht, *J. Phys. Chem. C*, 2013, **117**, 13403-13412.
13. H. Nakai, T. Kubota, A. Kita and A. Kawashima, *J. Electrochem. Soc.*, 2011, **158**, A798-A801.
14. Y. Chen, Y. Hu, Z. Shen, R. Chen, X. He, X. Zhang, Y. Zhang and K. Wu, *Electrochim. Acta*, 2016, **210**, 53-60.
15. W. Duan, Z. Zhu, H. Li, Z. Hu, K. Zhang, F. Cheng and J. Chen, *J. Mater. Chem. A*, 2014, **2**, 8668-8675.
16. P. Nie, Z. Le, G. Chen, D. Liu, X. Liu, H. B. Wu, P. Xu, X. Li, F. Liu, L. Chang, X. Zhang and Y. Lu, *Small*, 2018, **14**, 1800635.
17. C. Zhang, X. Cai, W. Chen, S. Yang, D. Xu, Y. Fang and X. Yu, *ACS Sus. Chem. Eng.*, 2018, **6**, 9930-9939.

18. D. Ji, Y. Wan, Z. Yang, C. Li, G. Xiong, L. Li, M. Han, R. Guo and H. Luo, *Electrochim. Acta*, 2016, **192**, 22-29.
19. T. Mu, P. Zuo, S. Lou, Q. Pan, Q. Li, C. Du, Y. Gao, X. Cheng, Y. Ma and G. Yin, *Chem. Eng. J.*, 2018, **341**, 37-46.
20. W. Sun, L. Wan, X. Li, X. Zhao and X. Yan, *J. Mater. Chem. A*, 2016, **4**, 10948-10955.
21. J. Xie, L. Tong, L. Su, Y. Xu, L. Wang and Y. Wang, *J. Power Sources*, 2017, **342**, 529-536.
22. J.-K. Yoo, J. Kim, Y. S. Jung and K. Kang, *Adv. Mater.*, 2012, **24**, 5452-5456.
23. Y.-C. Zhang, Y. You, S. Xin, Y.-X. Yin, J. Zhang, P. Wang, X.-s. Zheng, F.-F. Cao and Y.-G. Guo, *Nano Energy*, 2016, **25**, 120-127.
24. Y. Zhang, N. Du, Y. Chen, Y. Lin, J. Jiang, Y. He, Y. Lei and D. Yang, *Nanoscale*, 2018, **10**, 5626-5633.